Acoustic phonon dispersion and diffuse scattering across the valence transition of $(Pr_{0.85}Y_{0.15})_{0.7}Ca_{0.3}CoO_{3-\delta}$

D. Phelan,[1,*] M. J. Krogstad,[1] N. J. Schreiber,[1,2] R. Osborn,[1] A. H. Said,[3] H. Zheng,[1] and S. Rosenkranz[1]

[1]*Materials Science Division, Argonne National Laboratory, Lemont, Illinois 60439, USA*

[2]*Department of Materials Science and Engineering, Cornell University, Ithaca, New York 14853, USA*

[3]*Advanced Photon Source, Argonne National Laboratory, Lemont, Illinois 60439, USA*

(Received 10 June 2019; published 2 August 2019)

A number of praseodymium-containing cobalt perovskites undergo temperature-dependent metal-insulator transitions that involve a transfer of electrons between cobalt and praseodymium cations. We have used high-resolution inelastic x-ray scattering to directly measure the changes in the acoustic phonon dispersion through this transition in one such single crystal, $(Pr_{0.85}Y_{0.15})_{0.7}Ca_{0.3}CoO_{3-\delta}$, in an effort to understand the role of the lattice in the transition. Transverse and acoustic modes were measured in the pseudocubic (200), (220), and (222) zones both above and below the transition temperature. The resultant dispersion curves reveal that the transition is associated with a significant hardening of the pseudocubic C_{11} elastic constant, whereas C_{12} and C_{44} do not significantly change. Analysis of the temperature-dependent damping of the longitudinal acoustic mode in the (200) zone reveals a peak in the damping at temperatures just above the transition temperature. Significant elastic diffuse scattering is also observed above the transition temperature, likely resulting from clusters in which the electron transfer is beginning to occur as a precursor to the phase transition. The presence of these clusters likely limits the phonon lifetimes, thus leading to the observed damping.

DOI: 10.1103/PhysRevB.100.054101

I. INTRODUCTION

There is a long history of the study of magnetic and electronic properties of compounds that contain mixed or "intermediate"-valence rare-earth cations in which valence fluctuations influence the properties [1,2]. In some cases, the average rare-earth valence shifts as a function of an external variable such as temperature or pressure. This shift can be continuous or first-order, as in the case of samarium chalcogenides [3,4], for example. More recently, such phenomena have been observed in the double perovskites $Ba_2PrRu_{0.9}Ir_{0.1}O_6$ [5,6] as well as certain cobaltite perovskites, ($ACoO_3$), that contain praseodymium cations on the A-site. In the cobaltites, there is a first-order metal-insulator transition (MIT) on cooling [7], which is coupled to significant anomalies in the magnetic susceptibility, lattice constants, and heat capacity. This MIT was first reported for $Pr_{1/2}Ca_{1/2}CoO_3$ [7] but also occurs in various other similar compositions such as $(Pr_{1-y}Y_y)_{1-x}Ca_xCoO_3$ [8–16]. Common to this series of materials is a distinct change in the Pr valence that occurs at the MIT and has been observed in both x-ray absorption spectroscopy (XAS) [8,10,15,17–20] and electron energy loss spectroscopy [16]. These experiments are consistent with a concomitant change in the cobalt valence, indicative of a first-order shift in electron occupancy between sites, with the mean Pr valence increasing and the mean Co valence decreasing upon cooling. This electronic shift had been predicted by changes in the band structure determined by DFT calculations [21], which clearly show that the occupancy of the Pr $4f$ electrons is strongly coupled to the unit cell volume. In the low-temperature phase, Pr cations possess mixed valence, with the average between 3+ and 4+, whereas in the high-temperature phase the valence is 3+. XAS experiments also have been interpreted in terms of a simultaneous Co spin state transition occurring at the MIT [8,19,20].

At the first-order MIT temperature (T_{MIT}), these materials undergo a distinct change in unit cell volume, with the lattice parameters dropping to significantly smaller values in the low-temperature phase. This is thought to occur isomorphically, such that although the change in cell volume is anomalously large at T_{MIT}, the crystallographic space group (*Pnma*) does not change [7,22,23]. Recent single-crystal diffraction experiments are indeed consistent with this picture [15]. In itself, the isomorphic crystallographic transition is of interest as it is known to occur only in a few materials [24], including elemental cerium [25] and samarium chalcogenides [4]. The comparison of Pr cobaltites to samarium chalcogenides may be particularly appropriate because the volume collapse in the chalcogenides arises due to a shift in the samarium valence and a concomitant semiconductor-metal transition. For example, SmS undergoes a room-temperature isomorphic transition at 6.5 kbar upon increasing pressure in which Sm^{2+} transforms into Sm^{3+} and the resistivity drops [4]. Similar transitions upon cooling at ambient pressure were observed in $Sm_{1-x}Y_xS$ [26], where the Y substitution provides a source of chemical pressure.

Using inelastic neutron scattering, Mook *et al.* found evidence of strong coupling of the valence fluctuations to the phonons in both SmS and $Sm_{1-x}Y_xS$ [27–29]. Specifically, they noticed significant anomalies in the dispersion of the longitudinal acoustic (LA) modes, particularly for phonons

*Corresponding author: dphelan@anl.gov

propagating along [111]. These anomalies included (i) an anomalous upturn in the shape of the dispersion approximately 2/3 of the way to the zone boundary along [111], (ii) the fact that the LA phonons in the [111] branch were so soft that their energies were smaller than the transverse (TA) phonons except very close to the zone boundary, and (iii) an anomalous broadening of the line widths in the metallic phase. Some anomalies, such as softening, were observed in the longitudinal optic (LO) modes as well. In contrast, TA and transverse optic (TO) modes appeared relatively uncoupled to the change in valence. In a simplified picture, this can be understood because longitudinal modes are correlated with changes in interatomic distances (and hence lattice parameters) whereas transverse modes are not [27]. Anomalous softening of the [111] branch of the LA mode was also later reported by inelastic x-ray scattering experiments [30].

The identified coupling between valence fluctuations and phonons in the samarium chalcogenides motivates similar investigations to measure the phonon dispersion of Pr cobaltites in an effort to determine what role the lattice plays in the MIT and if and how the valence is coupled to the phonons. After all, despite the similarity of an isomorphic valence transition in both the Pr cobaltites and Sm chalcogenides, there are some notable differences such as the collapsed phases being metallic in the samarium chalcogenides but insulating in the cobaltites; thus, *a priori*, it is unclear how similar the coupling in the two systems is. To address this issue, we have performed inelastic x-ray scattering measurements to determine the acoustic phonon dispersion from a single crystal of $(Pr_{0.85}Y_{0.15})_{0.7}Ca_{0.3}CoO_{3-\delta}$, which undergoes a valence transition at $T_{MIT} \sim 135$ K under ambient pressure.

II. EXPERIMENT

Inelastic x-ray scattering experiments were performed on the HERIX instrument at Sector 30, 30-ID-C, of the Advanced Photon Source (APS) at Argonne National Laboratory. All inelastic measurements were taken as a function of energy transfer, $\hbar\omega$, with the wave-vector transfer, $\boldsymbol{Q}$, fixed (i.e., constant-$\boldsymbol{Q}$ scans). The energy resolution of HERIX, which has a full-width-at-half-maximum of ~1.5 meV, was measured using the elastic scattering from plastic and fit as a pseudo-Voigt function. This function was then convolved with the theoretical cross section during fitting of the experimental data to determine the inelastic scattering function, $S(\boldsymbol{Q},\omega)$, which is proportional to the measured intensity.

The inelastic x-ray scattering measurements were performed on a single crystal of $(Pr_{0.85}Y_{0.15})_{0.7}Ca_{0.3}CoO_3$. The crystal was grown by the floating zone method under high oxygen pressure and is in fact the same as previously reported in Ref. [15], where it was also shown via magnetometry and x-ray absorption spectroscopy that it undergoes the Pr valence transition in accordance with the bulk of the literature on polycrystalline samples. The oxygen stoichiometry has not been determined due to the reliance of the result on the accuracy of the metal cation stoichiometry. The crystal possesses an orthorhombic symmetry (see Ref. [23] for structural refinements of a similar composition) but was twinned as is usual for a perovskite with lower-than-cubic symmetry. Because of this, we are limited to a pseudocubic approximation of the symmetry over which the distinctions of the orthorhombic distortions are averaged over. As such, $\boldsymbol{Q}$ is specified throughout this manuscript by an aristotype perovskite cell with the pseudocubic lattice parameter, $a_{pc} \sim 3.78$ Å.

Measurements of the dispersion of both transverse acoustic (TA) and longitudinal acoustic (LA) phonon modes were performed in three different zones centered at the Bragg reflections, $\boldsymbol{\tau} = (200)$, (220), and (222). For $\boldsymbol{\tau} = (200)$, the TA mode that we measured has a reduced wave vector ($\boldsymbol{q} = \boldsymbol{Q} - \boldsymbol{\tau}$), $\boldsymbol{q}//[010]$ and an atomic displacement direction, $\boldsymbol{\xi}//[100]$; the LA mode has $\boldsymbol{q}//[100]$ and $\boldsymbol{\xi}//[100]$. For $\boldsymbol{\tau} = (220)$, the TA mode that we measured has $\boldsymbol{q}//[1\bar{1}0]$ and $\boldsymbol{\xi}//[110]$, and the LA mode has $\boldsymbol{q}//[110]$ and $\boldsymbol{\xi}//[110]$. Finally for $\boldsymbol{\tau} = (222)$, the TA mode that we measured has $\boldsymbol{q}//[1\bar{1}0]$, and $\boldsymbol{\xi}//[111]$ and the LA mode has $\boldsymbol{q}//[111]$ and $\boldsymbol{\xi}//[111]$.

Additional x-ray diffraction measurements were performed on a second single crystal at Sector 6-ID-D of the APS. The crystal was measured while in a nitrogen stream for temperature control. Measurements were performed using x-rays with incident energy of 87.1 keV. A Dectris Pilatus 2M CdTe detector was employed. The crystal was continuously rotated over 370° during the measurement at a rate of 1° per second, with 10 detector images collected per second in order to obtain the three-dimensional distribution of scattering over a wide wave-vector range. The data were symmetrized by employing $m\bar{3}m$ operations consistent with the Laue symmetry observed in the scattering. Analysis of the data was performed using NeXpy [31].

III. RESULTS AND DISCUSSION

We begin by considering the phonon measurements taken in the (200), (220), and (222) zones both above ($T = 160$ K) and below the transition ($T = 100$ K). An example of measurements of the TA mode in the (222) zone taken at these two temperatures is shown in Fig. 1. Significant hardening of the mode (increase of the energy at the same wave vector) is observed at 100 K compared to 160 K, indicating that the sound-wave velocity, which is given by the linear regime of $\frac{\partial\omega}{\partial q}$ in the small q (or, equivalently, the long-wavelength) limit of this mode, is increased at lower temperature. We fit $S(\boldsymbol{q},\omega)$ to that expected for a damped mode with an additional, resolution-limited elastic contribution. For a damped phonon, the imaginary part of the dynamic susceptibility (χ'') is given by [32]

$$\chi''_{\text{damped}}(\boldsymbol{q},\omega) = \frac{A\Gamma}{\pi}\left[\frac{1}{\Gamma^2+(\omega-\omega_0)^2} - \frac{1}{\Gamma^2+(\omega+\omega_0)^2}\right], \tag{1}$$

where Γ is the half-width-at-half-maximum of the two Lorentzians which corresponds to the energy width of the phonon at $\boldsymbol{q}$ that arises due to damping. A and ω_0 define the amplitude and energy of the phonon at $\boldsymbol{q}$. The phonon lifetime is inversely proportional to Γ, so finite values of Γ (i.e., line broadening beyond the spectral resolution) imply limited phonon lifetimes. The fluctuation-dissipation theorem then relates $\chi''(\boldsymbol{q},\omega)$ to $S(\boldsymbol{q},\omega)$ such that

$$\chi''_{\text{damped}}(\boldsymbol{q},\omega) = \pi[1 - e^{\frac{-\hbar\omega}{k_B T}}]S_{\text{damped}}(\boldsymbol{q},\omega). \tag{2}$$

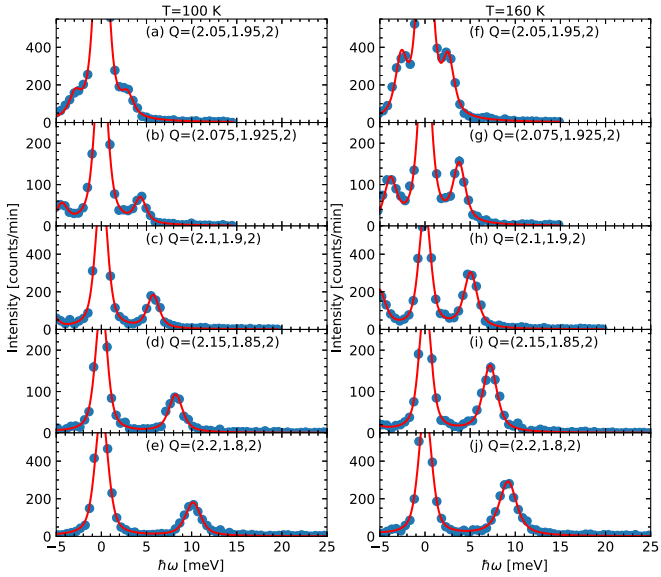

FIG. 1. Constant-$\boldsymbol{Q}$ scans of the transverse acoustic mode in the pseudocubic (222) zone. The solid red lines represent fits to a damped harmonic oscillator.

Our fitting function thus is

$$S_{\text{measured}}(\boldsymbol{q},\omega) = S_{\text{damped}}(\boldsymbol{q},\omega) + A_{\text{elastic}}(\boldsymbol{q})\delta(\omega), \quad (3)$$

where $A_{\text{elastic}}(\boldsymbol{q})$ represents the resolution-limited elastic cross section and the expression for $S_{\text{measured}}(\boldsymbol{q},\omega)$ is convoluted with the instrumental resolution.

By fitting the constant-$\boldsymbol{Q}$ scans in all three zones (see the Supplemental Material for similar constant-$\boldsymbol{Q}$ scans of the other five modes [33]), the acoustic phonon dispersion was thus determined at both $T = 160$ K and $T = 100$ K and is displayed in Fig. 2. Certain modes (e.g., the LA 200 mode) are significantly harder at 100 K, whereas other modes (e.g., the TA 200 mode) possess relatively little change. A listing of the six sound-wave velocities that were obtained at both

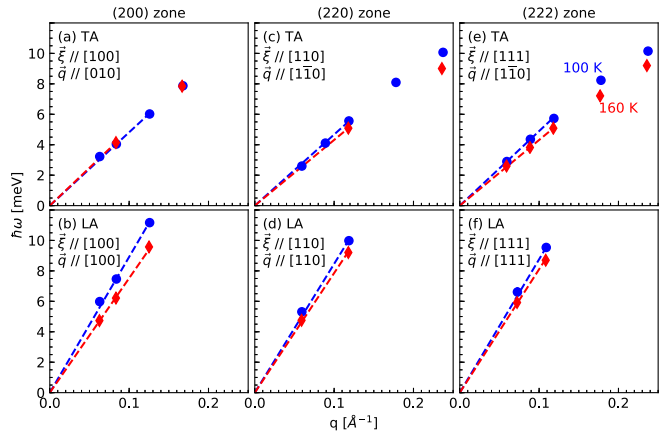

FIG. 2. Dispersion of the transverse and acoustic modes in the (a, b) (200), (c, d) (220), and (e, f) (222) pseudocubic zones at 100 K (blue circles) and 160 K (red diamonds). Dashed lines show the linear fit to the dispersion in the long-wavelength limit.

temperatures is provided in Table I. To make sense of these changes, we consider the temperature dependence of the elastic constants. We note that because of the twinning we are only able to evaluate the elastic constants in a pseudocubic approximation. In this approximation, there are three unique elastic constants (C_{11}, C_{12}, and C_{44}), and these are related to the sound wave velocities, v_{hkl}^{mode}, by the following equations [34]:

$$C_{11} = \rho\left[v_{200}^{LA}\right]^2, \quad (4)$$

$$C_{44} = \rho\left[v_{200}^{TA}\right]^2, \quad (5)$$

$$\tfrac{1}{2}(C_{11} + C_{12} + 2C_{44}) = \rho\left[v_{220}^{LA}\right]^2, \quad (6)$$

$$\tfrac{1}{2}(C_{11} - C_{12}) = \rho\left[v_{220}^{TA}\right]^2, \quad (7)$$

$$\tfrac{1}{3}(C_{11} + 2C_{12} + 4C_{44}) = \rho\left[v_{222}^{LA}\right]^2, \quad (8)$$

and

$$\tfrac{1}{3}[C_{11} - C_{12} + C_{44}] = \rho\left[v_{222}^{TA}\right]^2. \quad (9)$$

In Eqs. (4)–(9), the hkl subscripts of v_{hkl}^{mode} specify the zone, while the mode superscript specifies whether the mode is transverse or longitudinal acoustic, and ρ is the density of the crystal. We fit the measured velocities using these relations to obtain the three pseudocubic elastic constants at both $T = 160$ K and $T = 100$ K, which are given in Table II. From the fitting, as well as from the observations that there is essentially no change in the TA dispersion in the (200) mode but a large change in the LA dispersion, we see that C_{11} changes significantly (increases by about 33%), whereas C_{44} does not change significantly. C_{12} may change, but not nearly as much as C_{11}, and the change would be at the level of the uncertainty, so we cannot say definitively whether it does or does not. C_{11} relates an axial stress to strain along the same axis, and its change implies that the low-temperature phase is axially stiffer.

We now further examine the temperature dependence of the LA (200) and TA (222) modes, shown in Fig. 3. Each scan was fitted by Eq. (3), and the resultant parameters are shown in Fig. 4. A sharp increase in both the LA and TA phonon energy is observed upon cooling through T_{MIT} as is clearly seen in Figs. 4(a) and 4(c). Interestingly, although neither of these modes is strongly damped at these wave vectors, we observe a distinct temperature dependence to the width (Γ) of the LA (200) mode. In the metallic phase at 250 K, Γ is ~1.15 meV implying that the mode is slightly underdamped with a finite lifetime. As T_{MIT} is approached upon cooling, Γ increases to ~1.6 meV. It is maximal just above T_{MIT} and drops as T_{MIT} is passed and reaches 0.9 meV at 120 K, below which it remains constant. This temperature-dependent width evidences a correlation between the phonon lifetimes and the electrical properties and hence valence fluctuations. Thus, there is a correlation of the phonon lifetimes with the valence fluctuations, with the phonon lifetime of the LA (200) mode becoming minimal at a temperature just above T_{MIT}. The variance in the temperature dependence of the width of the TA

TABLE I. Sound velocities determined from the linear, low-$\boldsymbol{q}$ portion of the acoustic phonon dispersion. The uncertainties represent the standard deviation from the fitting.

Zone	Mode	Direction of $\boldsymbol{q}$	Direction of $\boldsymbol{\xi}$	$v_{160K}[10^5$ cm/s]	$v_{100K}[10^5$ cm/s]
(200)	TA	[010]	[100]	3.77 ± 0.02	3.66 ± 0.03
(200)	LA	[100]	[100]	5.71 ± 0.05	6.77 ± 0.08
(220)	TA	[1–10]	[110]	3.28 ± 0.02	3.55 ± 0.02
(220)	LA	[110]	[110]	5.97 ± 0.08	6.43 ± 0.12
(222)	TA	[1–10]	[111]	3.276 ± 0.001	3.719 ± 0.008
(222)	LA	[111]	[111]	6.16 ± 0.06	6.66 ± 0.04

mode at (2.15, 1.85, −2) was, on the other hand, at the level of the uncertainties from the fit such that no coupling of that mode width to the transition could be discerned.

Given that there are changes in the phonons at long wavelength, there are likely anomalies over a broader range of wave vectors. Measurements were taken at larger $\boldsymbol{q}$ extending out to the zone boundaries, but we found that the observed phonon cross sections become very broad and almost certainly result from the superposition of several modes (i.e., by a combination of acoustic and optic modes) as can be seen in Fig. 1 and in the supplemental figures [33]. This superposition complicates assessment of the dispersions of the modes and line widths at large $\boldsymbol{q}$. While several of these phonons clearly show temperature-dependent shifts, we do not discuss them in further detail because it is not possible to resolve the individual modes.

Interestingly, inspection of the temperature-dependent spectra in Fig. 3 reveals that not only the phonon energies harden in the low-temperature phase, but also that there are also clear changes in the elastic cross sections at both $\boldsymbol{Q} = (2.1, 0, 0)$ and $\boldsymbol{Q} = (2.15, 1.85, -2)$. Specifically, the elastic scattering at both of these wave vectors is significantly enhanced around T_{MIT}. We first attempted to add a quasielastic term to Eq. (3) to allow for a broadening of the elastic line but found that the enhancement is elastic within the energy resolution of the experiment (though fluctuations at sub-meV energies cannot be ruled out). Since the enhancement of the elastic line is well displaced from the Bragg reflections at both wave vectors, this intensity is elastic diffuse scattering. In order to characterize the temperature dependence of this diffuse scattering more precisely, we measured the scattering at (2.1,0,0) as a function of temperature with the spectrometer aligned on the elastic line, as shown in Fig. 5. The diffuse scattering increases steadily below 180 K and forms a relatively sharp peak in temperature at T_{MIT} and then drops back down as the temperature is further decreased. This temperature dependence is reminiscent of critical scattering that is observed in second-order phase transitions, such as that observed around paramagnetic-ferromagnetic phase transitions. However, in the present case the transition is known to be first-order. Moreover, in the case of second-order transitions, the scattering is inelastic, whereas here it is elastic. Thus, in these ways, the diffuse scattering differs from critical scattering.

To further understand the origins of the diffuse scattering, additional measurements were performed at Sector 6 of the APS. The use of an area detector allowed for observation of $S(\boldsymbol{Q})$ over a large volume of wave-vector space. It is important to note that, whereas the measurements on HERIX have energy discrimination, the measurements on Sector 6 do not. The observed intensities contain both the elastic and the inelastic contributions, which cannot be resolved; nevertheless, they are still useful for determining the shape of the diffuse scattering over a large volume of reciprocal space. Figure 6(a) shows an example of the diffuse scattering at 130 K in the pseudocubic $(hk0)$ scattering plane. In addition to the strong Bragg peaks, a weak, diffuse pattern is observed. To extricate the part of the diffuse signal that varies with temperature, the diffuse signal at low temperature

TABLE II. Pseudocubic elastic constants determined from measurements of the acoustic phonon dispersion at 100 K and 160 K. The uncertainties represent the standard deviation from fitting.

T [K]	$C_{11}[10^{11}\,\mathrm{Nm}^{-2}]$	$C_{12}[10^{11}\,\mathrm{Nm}^{-2}]$	$C_{44}[10^{11}\,\mathrm{Nm}^{-2}]$
160	2.20 ± 0.20	0.92 ± 0.19	0.90 ± 0.06
100	2.94 ± 0.16	1.13 ± 0.14	0.96 ± 0.06

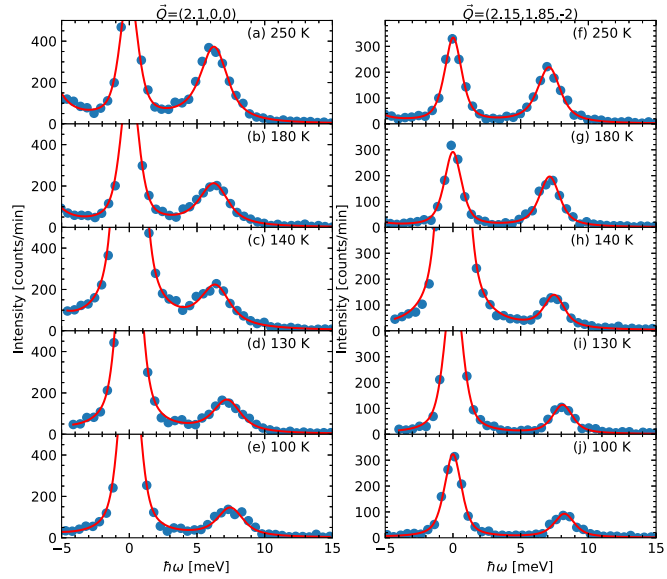

FIG. 3. Temperature-dependent constant-$\boldsymbol{Q}$ scans of the (a–e) longitudinal acoustic mode at (2.1,0,0) and the (f–j) transverse acoustic mode at (2.15,1.85,−2). The solid red lines represent fits as described in the text. Uncertainties in the measured intensities are smaller than the size of the symbols used to show the data.

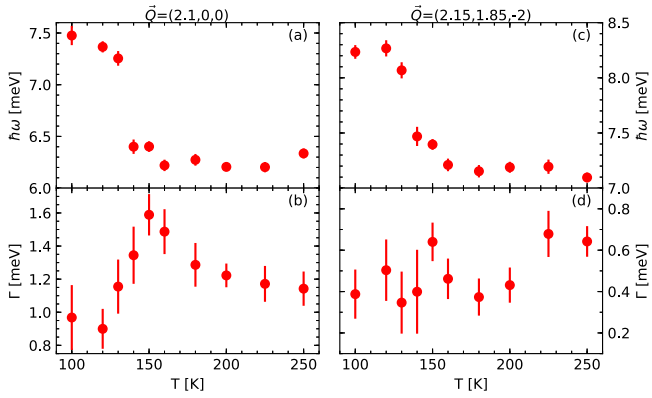

FIG. 4. Results from the fitting of the constant-$\boldsymbol{Q}$ scans of the longitudinal acoustic mode at (2.1,0,0) and the transverse acoustic mode at (2.15,1.85,−2). The phonon energy, $\hbar\omega$, is shown in panels (a) and (c), at (2.1,0,0) and (2.15,1.85,−2), respectively, while the width, Γ, is shown in panels (b) and (d), at (2.1,0,0) and (2.15,1.85,−2), respectively.

(110 K) was subtracted from the signal just above T_{MIT} (150 K). We note that the subtraction was performed upon data in reciprocal lattice units and that the reciprocal lattice unit was adjusted at both temperatures to account for the temperature variation in the pseudocubic lattice constant. Thus, the temperature-subtracted signal informs how the local atomic deviations from the average high-temperature structure (150 K) differ from the local atomic deviations from the average low-temperature structure (110 K), but they do not directly inform the change in structure since the average high- and low-temperature structures are different. Figure 6(b) shows the temperature-subtracted intensity in the (hk0) plane. There are large swaths of reciprocal space (which appear red) that possess stronger diffuse scattering at high temperature, and other swaths (which appear blue) that possess weaker diffuse scattering at high temperature. These broad features appear similar to classic "size-effect" diffuse scattering, where the symmetry-breaking local structure accommodates differently sized cations that occupy crystallographically equivalent

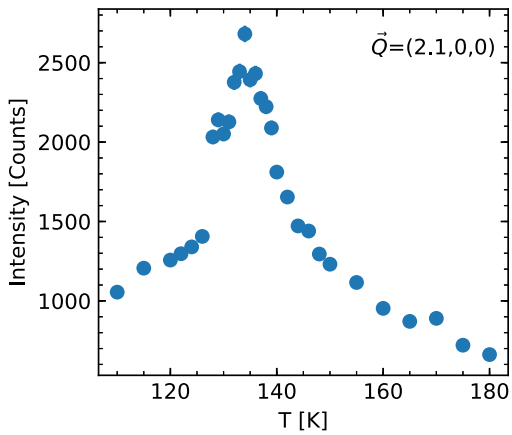

FIG. 5. Temperature dependence of the elastic scattering at (2.1,0,0).

positions [35]. In the present case, we note that there are three different atomic species that occupy the A-site (Pr, Ca, and Y), and moreover that we have to consider two different Pr valence states (3+ and 4+) which have differently sized radii. On the B-site, there are different cobalt valence states (3+ and 4+), with different radii as well as the potential for different Co^{3+} spin states which also have unique radii. Thus, there are many potential sources of size-effect scattering, though the most dominant contribution is likely from Pr because it has the most electrons and is thus by far the dominant scatterer.

It is useful for understanding the diffuse scattering to consider the three-dimensional difference pair distribution function (3D-ΔPDF), which is the Fourier transform of the diffuse scattering at a particular temperature with the average structure subtracted out by removal of the primary Bragg reflections [36,37]. The 3D-ΔPDF is a function of a real space vector $\vec{r}$ connecting a pair of atoms. Positive values of the 3D-ΔPDF describe correlations more likely than average to be present in the local structure, and negative values describe correlations less likely to occur, each weighted by the form factor. Additional details regarding the generation of the 3D-ΔPDFs can be found in the Supplemental Material [33].

Figure 6(c) shows the 3D-ΔPDF at 130 K. A key feature is the split negative and positive intensities centered at $\vec{r} = [1, 0, 0]$, which connects an atom in a particular pseudocubic cell to the atom at the same position in the next pseudocubic cell. This feature is indicative of "size-effect" scattering, where the average distance between two atoms on crystallographic sites connected by a given real-space vector is dependent on the distinct types of atoms occupying those sites. Co-Co and O-O pairs can be eliminated as the source of this 3D-ΔPDF signal because there are only single-atom types on the Co and O sites. As the only crystallographic site with distinct occupants, this suggests the distance between A-site nearest neighbors differs depending on their atom type. The positive intensity at $\vec{r} = [1 + \delta, 0, 0]$ indicates that nearest-neighbor Pr-Pr distances are likely to be larger than one lattice unit, while the negative intensity observed at $\vec{r} = [1 - \delta, 0, 0]$ indicates that nearest-neighbor distances between lighter atomic pairs are likely to be smaller than one lattice unit.

By creating 3D-ΔPDFs at various temperatures, the temperature dependence of the local long correlations can be assessed. Figure 6(e) tracks the positive and negative correlations at 1+δ and 1-δ. A clear anomaly is observed at T_{MIT}, below which the probabilities of these correlations steadily increases. If we attribute these features to Pr-Pr pairs, as suggested above, then this implies that long, symmetry-breaking nearest-neighbor Pr-Pr correlations tend to increase in quantity below T_{MIT}. A splitting of pair correlations was also observed in the 3D-ΔPDF at $\vec{r} = [1/2, 1/2, 1/2]$, as shown in Fig. 2(d). This correlation corresponds only to nearest-neighboring Co-(Pr/Y/Ca) pairs. We again see that an axially longer length is positively correlated, and a shorter length is negatively correlated. By similar arguments as above, these correlations are dominated by Co-Pr pairs. As the temperature is lowered, an anomaly is again observed in the positive and negative correlations; however, in this case at low temperature the probabilities of these correlations is diminished below T_{MIT}. Although we lack a complete understanding of the mechanisms of the local distortions, it is clear that correlations

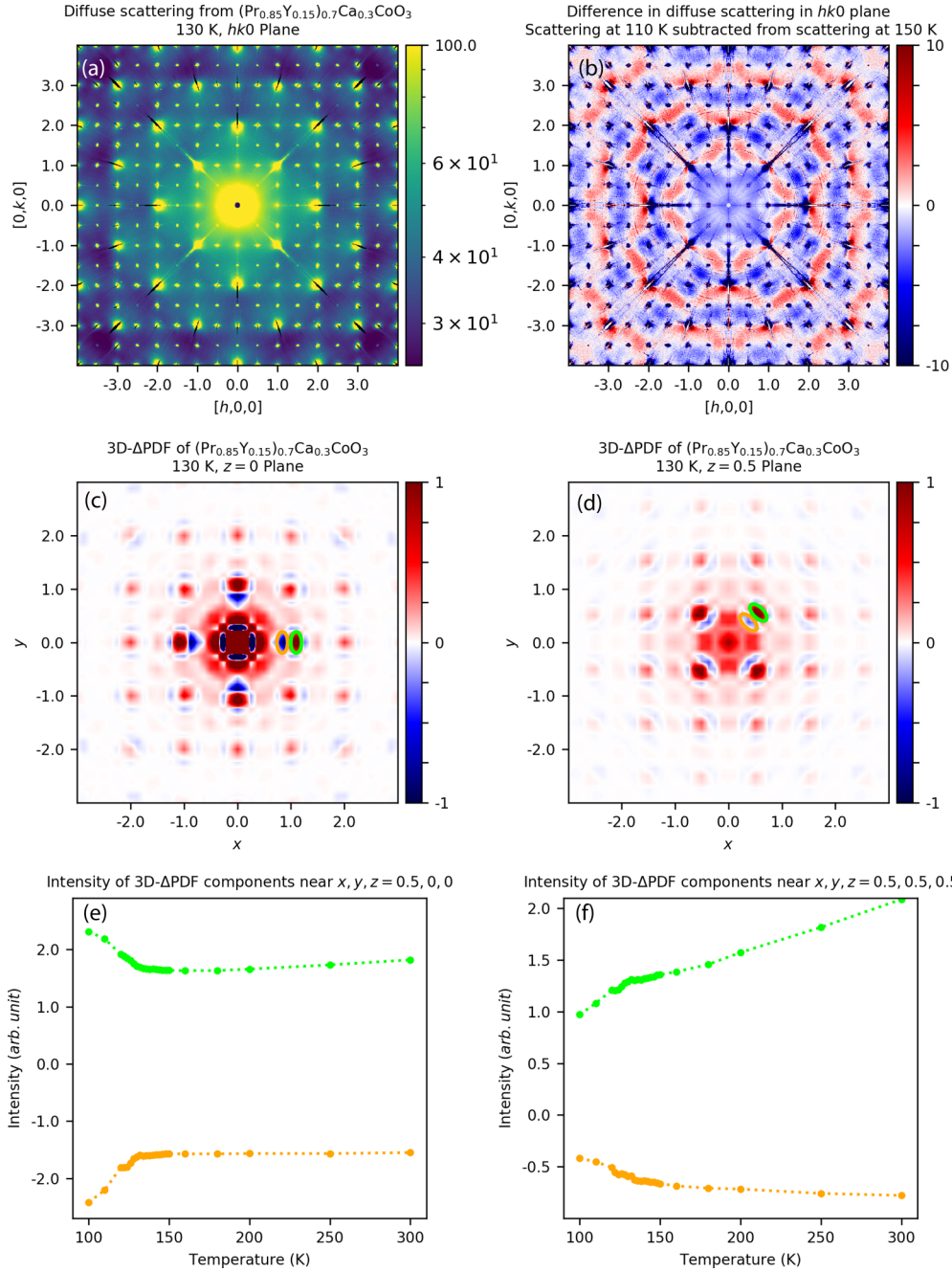

FIG. 6. (a) X-ray scattering in the (*hk*0) plane at 130 K shows diffuse features. (b) The low-temperature (110 K) diffuse scattering is subtracted from the 150 K scattering. (c) The 3D-ΔPDF in the $z = 0$ plane. The long-pair correlation is circled in green, and the short-pair correlation is circled in orange. (d) The 3D-ΔPDF in the $z = 1/2$ plane. The long-pair correlation is circled in green, and the negative short-pair correlation is circled in orange. (e) The temperature dependence of the positive and negative correlations depicted in panel (c) are shown in green and orange, respectively. (f) The temperature dependence of the positive and negative correlations depicted in panel (d) are shown in green and orange, respectively.

involving Pr cations show anomalous temperature-dependent splitting that is tied to the metal-insulator transition and shift of valence.

The observation of the critical-like diffuse scattering above T_{MIT} indicates that there is a breaking of the long-range symmetry on local length scales as T_{MIT} is approached from above and clearly indicates that these distortions are precursors to the phase transition. This is surprising for a transition that is first-order. However, we note that it is reminiscent of the body of work on martensitic phase transitions [38] (e.g., TiNi), which show clear evidence of diffuse scattering as a precursor above the phase transition. We speculate that in the present case, the source of the short-range order are regions or clusters above T_{MIT} in which the valence has begun to shift. This interpretation is consistent with the XAS measurements of Fujishiro *et al.*, who showed that the charge transfer between Pr and Co occurs above T_{MIT} and occurs gradually [8]. The existence of such distortions may lead to the dampening

of the phonons which is maximal near T_{MIT} as discussed above.

IV. SUMMARY

We have determined the dispersion of the long-wavelength acoustic modes both above and below T_{MIT} for $(Pr_{0.85}Y_{0.15})_{0.7}Ca_{0.3}CoO_{3-\delta}$ and determined the TA and LA sound wave velocities along the [100], [110], and [111] pseudocubic directions. Significant changes in certain sound wave velocities can be rationalized in terms of changes in the C_{11} pseudocubic elastic constant. The phonon energies and line widths have been determined as a function of temperature through the phase transition, and coupling of the line widths to the valence transition is evidenced. Surprisingly, significant elastic critical-like scattering is present above T_{MIT} and becomes maximal near T_{MIT}. This diffuse scattering, reminiscent of that observed around martensitic phase transitions, arises from precursor local lattice deformations above T_{MIT}, which may arise from precursor changes in the Pr valence state, consistent with XAS measurements. Local pair correlations involving Pr atoms exhibit deviations from the average structure as evidenced in the 3D-ΔPDFs. Such distortions may lead to the observed damping of certain phonons.

ACKNOWLEDGMENTS

Work in the Materials Science Division at Argonne National Laboratory was supported by the US Department of Energy, Office of Science, Basic Energy Sciences, Materials Science and Engineering Division. This research used resources of the Advanced Photon Source, a US Department of Energy (DOE) Office of Science User Facility operated for the DOE Office of Science by Argonne National Laboratory under Contract No. DE-AC02-06CH11357. The authors thank Prof. Chris Leighton for valuable discussion.

[1] R. D. Parks, editor, *Valence Instabilities and Related Narrow Band Phenomena* (Plenum Press, New York, 1977).
[2] J. M. Lawrence, P. S. Riseborough, and R. D. Parks, Rep. Prog. Phys. **44**, 1 (1981).
[3] A. Sousanis, P. F. Smet, and D. Poelman, Materials (Basel) **10**, 953 (2017).
[4] A. Jayaraman, V. Narayanamurti, E. Bucher, and R. G. Maines, Phys. Rev. Lett. **25**, 1430 (1970).
[5] M. Wakeshima, Y. Izumiyama, Y. Doi, and Y. Hinatsu, Solid State Commun. **120**, 273 (2001).
[6] J. Sannigrahi, D. T. Adroja, C. Ritter, W. Kockelmann, A. D. Hillier, K. S. Knight, A. T. Boothroyd, M. Wakeshima, Y. Hinatsu, J. F. W. Mosselmans, and S. Ramos, Phys. Rev. B **99**, 184440 (2019).
[7] S. Tsubouchi, T. Kyômen, M. Itoh, P. Ganguly, M. Oguni, Y. Shimojo, Y. Morii, and Y. Ishii, Phys. Rev. B **66**, 052418 (2002).
[8] H. Fujishiro, T. Naito, S. Ogawa, N. Yoshida, K. Nitta, J. Hejtmánek, K. Knížek, and Z. Jirák, J. Phys. Soc. Jpn. **81**, 064709 (2012).
[9] T. Fujita, T. Miyashita, Y. Yasui, Y. Kobayashi, M. Sato, E. Nishibori, M. Sakata, Y. Shimojo, N. Igawa, Y. Ishii, K. Kakurai, T. Adachi, Y. Ohishi, and M. Takata, J. Phys. Soc. Jpn. **73**, 1987 (2004).
[10] J. Hejtmánek, E. Šantavá, K. Knížek, M. Maryško, Z. Jirák, T. Naito, H. Sasaki, and H. Fujishiro, Phys. Rev. B **82**, 165107 (2010).
[11] M. Maryško, Z. Jirák, K. Knížek, P. Novák, J. Hejtmánek, T. Naito, H. Sasaki, and H. Fujishiro, J. Appl. Phys. **109**, 07E127 (2011).
[12] T. Naito, H. Fujishiro, T. Nishizaki, N. Kobayashi, J. Hejtmánek, K. Knížek, and Z. Jirák, J. Appl. Phys. **115**, 233914 (2014).
[13] Y. Noda, H. Fujishiro, T. Naito, A. Ito, T. Goto, J. Hejtmanek, and Z. Jirak, AIP Adv. **6**, 025318 (2016).
[14] D. Phelan, K. P. Bhatti, M. Taylor, S. Wang, and C. Leighton, Phys. Rev. B **89**, 184427 (2014).
[15] N. J. Schreiber, J. Zhang, H. Zheng, J. W. Freeland, Y. S. Chen, J. F. Mitchell, and D. Phelan, J. Solid State Chem. **254**, 69 (2017).
[16] A. Gulec, D. Phelan, C. Leighton, and R. F. Klie, ACS Nano **10**, 938 (2016).
[17] J. Herrero-Martín, J. L. García-Muñoz, S. Valencia, C. Frontera, J. Blasco, A. J. Barón-González, G. Subías, R. Abrudan, F. Radu, E. Dudzik, and R. Feyerherm, Phys. Rev. B **84**, 115131 (2011).
[18] J. L. García-Muñoz, C. Frontera, A. J. Barón-González, S. Valencia, J. Blasco, R. Feyerherm, E. Dudzik, R. Abrudan, and F. Radu, Phys. Rev. B **84**, 045104 (2011).
[19] J. Herrero-Martín, J. L. García-Muñoz, K. Kvashnina, E. Gallo, G. Subías, J. A. Alonso, and A. J. Barón-González, Phys. Rev. B **86**, 125106 (2012).
[20] F. Guillou, Q. Zhang, Z. Hu, C. Y. Kuo, Y. Y. Chin, H. J. Lin, C. T. Chen, A. Tanaka, L. H. Tjeng, and V. Hardy, Phys. Rev. B **87**, 115114 (2013).
[21] K. Knížek, J. Hejtmánek, P. Novák, and Z. Jirák, Phys. Rev. B **81**, 155113 (2010).
[22] P. Tong, Y. Wu, B. Kim, D. Kwon, J. M. S. Park, and B. G. Kim, J. Phys. Soc. Jpn. **78**, 034702 (2009).
[23] K. Knížek, J. Hejtmánek, M. Maryško, P. Novák, E. Šantavá, Z. Jirák, T. Naito, H. Fujishiro, and C. de la Cruz, Phys. Rev. B **88**, 224412 (2013).
[24] J. F. Scott, Adv. Mater. **22**, 2106 (2010).
[25] B. Johansson, W. Luo, S. Li, and R. Ahuja, Sci. Rep. **4**, 6398 (2014).
[26] S. von Molnar, T. Penney, and F. Holtzberg, J. Phys. Colloques **37**, C4-241 (1976).
[27] H. A. Mook, R. M. Nicklow, T. Penney, F. Holtzberg, and M. W. Shafer, Phys. Rev. B **18**, 2925 (1978).
[28] H. A. Mook and R. M. Nicklow, Phys. Rev. B **20**, 1656 (1979).
[29] H. A. Mook, D. B. McWhan, and F. Holtzberg, Phys. Rev. B **25**, 4321 (1982).
[30] S. Raymond, J. P. Rueff, M. D'Astuto, D. Braithwaite, M. Krisch, and J. Flouquet, Phys. Rev. B **66**, 220301(R) (2002).
[31] R. Osborn, https://github.com/nexpy/nexpy.
[32] C. Stock, H. Luo, D. Viehland, J. F. Li, I. P. Swainson, R. J. Birgeneau, and G. Shirane, J. Phys. Soc. Jpn. **74**, 3002 (2005).

[33] See Supplemental Material at http://link.aps.org/supplemental/10.1103/PhysRevB.100.054101 for additional constant-$\boldsymbol{Q}$ scans and a description of the 3D-ΔPDF analysis.
[34] Y. Noda, Y. Yamada, and S. M. Shapiro, Phys. Rev. B **40**, 5995 (1989).
[35] T. R. Welberry and B. D. Butler, J. Appl. Crystallogr. **27**, 205 (1994).
[36] M. J. Krogstad, S. Rosenkranz, J. M. Wozniak, G. Jennings, J. P. C. Ruff, J. T. Vaughey, and R. Osborn, arXiv:1902.03318 [Nature Materials (to be published)].
[37] T. Weber and A. Simonov, Zs. Krist. **227**, 238 (2012).
[38] K. Chandra and G. R. Purdy, J. Appl. Phys. **39**, 2176 (1968).